Nonlinear Evolution of the AdS_{4} Superradiant Instability

Paul M. Chesler and David A. Lowe

Nonlinear evolution of the AdS$_4$ superradiant instability

Paul M. Chesler

Black Hole Initiative, Harvard University, Cambridge, MA 02138, USA[*]

David A. Lowe

Department of Physics, Brown University, Providence, RI 02912, USA [†]
(Dated: April 16, 2019)

The superradiant instability of rotating black holes with negative cosmological constant is studied by numerically solving the full 3+1-dimensional Einstein equations. We find evidence for an epoch dominated by a solution with a single helical Killing vector and a multi-stage process with distinct superradiant instabilities.

Introduction.— Energy may be extracted from rotating black holes via scattering involving superradiant modes [1]. It was suggested some time ago that if such modes could be confined using a mirror, then an amplification process can occur, leading to a significant fraction of the rest mass of the black hole being converted into radiation [1, 2]. This process — coined the black hole bomb — arises in a diverse set of fields including early universe cosmology [3], particle physics and gravitational wave astrophysics [4, 5], astrophysical jets [6], and via holographic duality [7], condensed matter physics [8]. For a detailed review see [6]. In the present work we study the black hole bomb with gravitational waves and replace the mirror by a negative cosmological constant and asymptotically AdS boundary conditions. The geometry then contains a time-like boundary from which gravitational waves can reflect off and the resulting Kerr-AdS black holes [9] can be unstable [10]. Aside from numerical convenience, the asymptotically AdS boundary conditions also mean that the system has a dual holographic interpretation as a strongly coupled quantum field theory living on the boundary.

Earlier work studied this problem perturbatively around the Kerr-AdS solution, where the quasi-normal modes have been studied in detail [11]. However up until now it has been difficult to study the nonlinear amplification mechanism in the full 3+1-dimensional case. Consequently, the final fate of the instability remains unknown. Progress has been made in some analog problems with more symmetry, such as Reissner-Nordstrom black holes coupled to charged scalars [12, 13] with spherical symmetry, and massive complex vector bosons coupled to Kerr with axisymmetric geometry [5].

For given mass and angular momentum, it was demonstrated in Ref. [14] that there exists "black resonator" solutions to Einstein's equations with higher entropy than Kerr-AdS. These are time-periodic black hole solutions with a single helical Killing vector. Since these solutions have higher entropy, it is possible they could be the endpoint of the instability. However, they are also unstable to superradiant instabilities [15]. This led Ref. [16] to speculate the evolution of the system could be that of a cascade, with the Kerr-AdS geometry transitioning to a black resonator, which then subsequently transitions to another black resonator and so on. Time evolution could lead to ever increasing structure on short distance scales, potentially violating cosmic censorship [16].

We numerically evolve the $3 + 1$ dimensional Einstein equations and find evolution consistent with the transition of Kerr-AdS to a black resonator. Specifically, we find that the Kerr-AdS geometry undergoes the expected superradiant instability, but then transitions to a solution with an approximate helical Killing vector. This solution then undergoes a new and distinct superradiant instability, with the most unstable mode having both shorter wavelength and smaller growth rate than that in Kerr-AdS. In the dual field theory, we find that the black resonator instability leads to an exotic state, with regions of negative energy persisting for long periods of time. We do not evolve to the endpoint of the black resonator instability, leaving the issue of the endpoint unresolved.

Setup.—We numerically solve the vacuum Einstein equations with negative cosmological constant $\Lambda = -3/L^2$ with L the AdS radius, which we set to one. Our numerical algorithm is largely described in [17]. We employ a characteristic evolution scheme with metric anzatz

$$ds^2 = r^2 g_{\mu\nu}(x^\alpha, r)dx^\mu dx^\nu + 2dtdr, \qquad (1)$$

with Greek indices (μ, ν) running over the AdS boundary spacetime coordinates $x^\mu = \{t, \theta, \varphi\}$ where θ and φ are the usual polar and azimuthal angles in spherical coordinates. The coordinate r is the AdS radial coordinate, with the AdS boundary located at $r = \infty$. The ansatz (1) is invariant under the residual diffeomorphism $r \to r + \xi(x^\alpha)$ with arbitrary $\xi(x^\alpha)$. We exploit this to fix the location of the apparent horizon to be at $r = 1$ and restrict the computation domain to $r \geq 1$.

The AdS boundary is time-like and hence requires the imposition of boundary conditions there. Near the AdS boundary one can solve Einstein's equations with a power series expansion. Doing so one obtains $g_{\mu\nu}(x, r) = g_{\mu\nu}^{(0)}(x) + \cdots + g_{\mu\nu}^{(3)}(x)/r^3 + \dots$. The expansion coefficient $g_{\mu\nu}^{(0)}$ corresponds to the metric on AdS boundary,
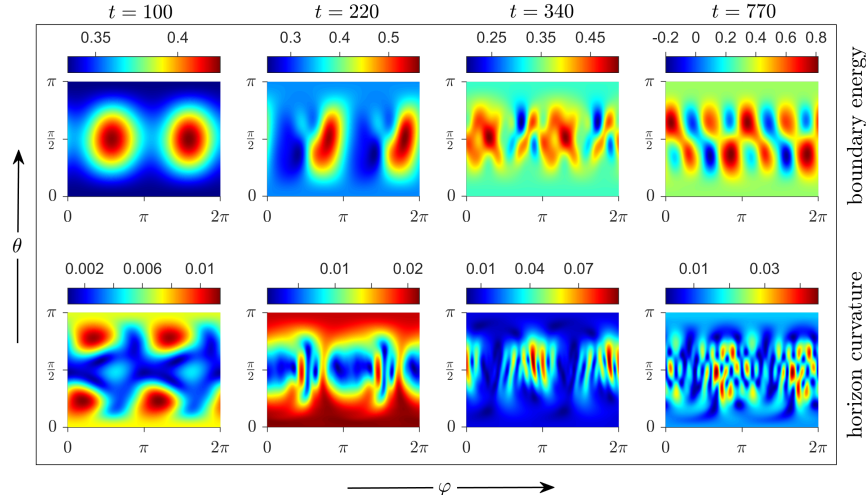
FIG. 1: Top: the boundary energy density T^{00} at four different times. Bottom: $\sqrt{K_{MN}K^{MN}}$, with K_{MN} the horizon extrinsic curvature, plotted at the same times.

which we choose to be that of the unit sphere $h_{\mu\nu} = \mathrm{diag}(-1, 1, \sin^2\theta)$. A convenient diffeomorphism invariant observable is the stress tensor in the dual boundary quantum field theory, which reads [18]

$$T_{\mu\nu} = g_{\mu\nu}^{(3)} + \tfrac{1}{3} h_{\mu\nu} g_{00}^{(3)}. \tag{2}$$

For initial data we choose the Kerr-AdS solution with mass $M = 0.2783$ and angular momentum $J = 0.06350$. Additionally, we add small perturbations to seed the superradiant instability. See the Supplementary Material for details on our discretization scheme and the seed perturbations. We evolve 915 AdS radii in time.

Results and discussion.— In the top panel of Fig. 1 we plot snapshots of boundary energy density T^{00} at times $t = 100, 240, 340$ and 770. Note that the color scaling is different at each time. As we shall discuss further below, during $100 \lesssim t \lesssim 400$ the energy density rotates in φ at angular velocity $\mathcal{W} \approx 1.7$. Over longer time scales structure gradually builds up. At $t = 100$ there is clearly a mode with azimuthal quantum number $m = 2$ excited, with two peaks separated by angle $\Delta\varphi \approx \pi$. The amplitude of this mode is initially small, with the energy density deviating from uniformity in φ by only $\sim 15\%$ at $t = 100$. At $t = 220$, the two maxima have become distorted and grown in amplitude. At $t = 340$, additional maxima have begun to form. By $t = 770$ there is clearly an $m = 4$ excitation in the energy density, with four maxima and minima both above and below the equator, with adjacent maxima separated by $\Delta\varphi \approx \pi/2$. In contrast to time $t = 100$, at $t = 770$ the variation in the energy density is large. Indeed, the energy density in the minima is negative. Negative energy density indicates an exotic state of matter in the dual quantum field theory. Regions of negative energy density have also been seen

channel	$\mathcal{F}^{122}$	$\mathcal{F}^{222}$	$\mathcal{F}^{133}$	$\mathcal{F}^{233}$	$\mathcal{F}^{144}$	$\mathcal{F}^{244}$
$\mathrm{Re}\,\omega$	2.52	3.38	3.74	4.55	4.83	5.64
$\mathrm{Im}\,\omega \times 10^2$	0.424	2.25	0.0218	0.136	0.00108	0.00710

TABLE I: Frequencies for some unstable modes in Kerr-AdS with mass $M = 0.2783$ and angular momentum $J = 0.06350$.

in the holographic theories studied in [19–22].

The growth of structure is also evident on the horizon. One quantity to consider is the extrinsic curvature K_{MN} of the apparent horizon (with upper case latin indices running over bulk spacetime coordinates). The extrinsic curvature can be constructed from the null normal n_M to the horizon and an auxiliary null vector ℓ_M chosen to satisfy $\ell_M n^M = -1$. The extrinsic curvature is then given by $K_{MN} = \Pi^P_M \Pi^Q_N \nabla_P n_Q$ where the projector $\Pi^M_N = \delta^M_N + \ell^M n_N$. As the horizon is at $r \approx 1$ [25], we choose $n_M dx^M = dr$ and $\ell_M dx^M = -dt$. In the bottom panel of Fig. 1 we plot snapshots of $\sqrt{K^{MN}K_{MN}}$, again at times $t = 100, 240, 340$ and 770.

To elucidate the growth of different modes we study the evolution of the spherical harmonic transform of the boundary momentum density $\mathcal{F}^{s\ell m} \equiv \int d\Omega \, \mathcal{V}_i^{*s\ell m} T^{0i}$, with vector spherical harmonics $\mathcal{V}_i^{s\ell m}$ given by [23] $\mathcal{V}_i^{1\ell m} = \frac{1}{\sqrt{\ell(\ell+1)}} \nabla_i y^{\ell m}$ and $V_i^{2\ell m} = \frac{1}{\sqrt{\ell(\ell+1)}} \epsilon_i{}^j \nabla_j y^{\ell m}$. Here $\epsilon_i{}^j$ has non-zero components $\epsilon_\theta{}^\varphi = \csc\theta$ and $\epsilon_\varphi{}^\theta = -\sin\theta$, and $y^{\ell m}$ are spherical harmonics. The $s = 1, 2$ modes encode the longitudinal (or "electric") and transverse (or "magnetic") components of the momentum density, respectively.

In Fig. 2 we plot $|\mathcal{F}^{s\ell m}|$ for $m = 2, 4, 6$ (left, middle, right columns) and $\ell = m$ (blue), $\ell = m + 1$ (red) and $\ell = m + 2$ (green). The top row of plots shows the trans-
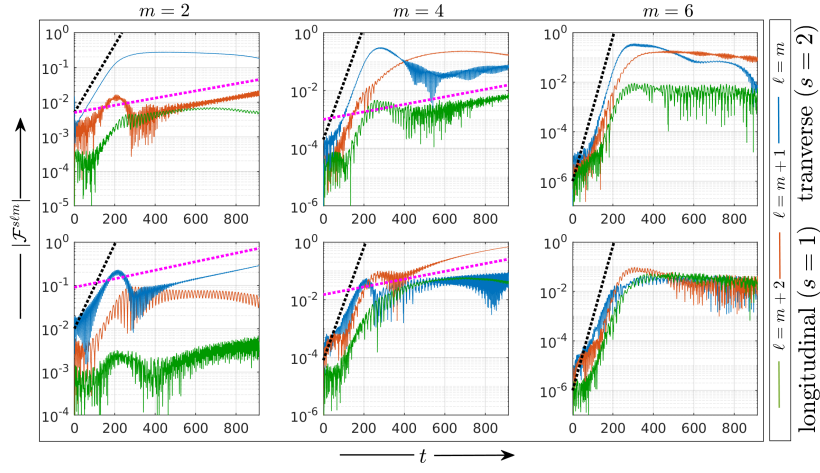
FIG. 2: $|\mathcal{F}^{s\ell m}|$ as a function of time for $m = 2, 4, 6$ and $\ell = m, m+1$ and $m+2$. Note the appearance of two distinct periods of exponential growth before $t \sim 200$ and after $t \sim 300$. Also shown as dashed black lines are $e^{\mathrm{Im}\,\omega_{222}t}$, $e^{2\mathrm{Im}\,\omega_{222}t}$ and $e^{3\mathrm{Im}\,\omega_{222}t}$ for $m = 2, 4, 6$, respectively, with ω_{222} the complex frequency of the transverse $\ell = m = 2$ unstable mode of Kerr-AdS. In the transverse channel, the pink dashed lines show $e^{0.0024t}$ for $m = 2$ and $e^{0.003t}$ for $m = 4$, respectively. In the longitudinal channel the dashed pink lines show $e^{0.0023t}$ and $e^{0.0031t}$ for $m = 2, 4$, respectively.

verse channel $|\mathcal{F}^{2\ell m}|$ while the bottom row of plots shows the longitudinal channel $|\mathcal{F}^{1\ell m}|$. The rapid oscillations seen in the plots are not numerical noise, but rather due to structure present on short time scales. Over large time scales there are two distinct periods of growth in $\mathcal{F}^{s\ell m}$, which we shall refer to as primary and secondary. The primary growth occurs until $t \sim 200$ and the secondary growth occurs after $t \sim 300$ and is slower than the primary growth. As we shall see below, the primary growth is driven by the leading linear instability in the Kerr-AdS geometry, the $\ell = m = 2$ mode in the transverse channel.

A linearized mode analysis about our choice of Kerr-AdS black hole yields a tower of unstable modes parameterized by ℓ and m in both the transverse and longitudinal channels [11]. The associated complex frequencies for the most unstable modes are given in Table I. From the table we see that the dominant unstable mode is that of the $\ell = m = 2$ mode in the transverse channel with complex frequency $\omega_{222} \approx 3.38 + 0.025i$. This mode grows more than 5 times faster than the next subdominant mode. Also included in Fig. 2 are plots of $e^{\mathrm{Im}\,\omega_{222}\,t}$, $e^{2\mathrm{Im}\,\omega_{222}\,t}$ and $e^{3\mathrm{Im}\,\omega_{222}\,t}$ in the $m = 2, 4, 6$ columns, respectively. These curves are shown as the dashed black lines in each plot. During the primary growth we clearly see $|\mathcal{F}^{222}| \sim e^{\mathrm{Im}\,\omega_{222}\,t}$, indicating growth consistent with a linearized analysis. At $t \sim 200$, when the primary growth begins to slow, $|\mathcal{F}^{222}|$ has grown to ~ 0.1. Evidently, the linearized analysis breaks down at this point, with $|\mathcal{F}^{222}|$ subsequently plateauing and slowly decreasing thereafter. For the $m = 4$ and $m = 6$ modes, we see $|\mathcal{F}^{244}| \sim e^{2\mathrm{Im}\,\omega_{222}\,t}$ and $|\mathcal{F}^{266}| \sim e^{3\mathrm{Im}\,\omega_{222}\,t}$ until $t \sim 200$, after which both modes begin to decrease in magnitude. This behavior is expected from perturba-

tion theory, where quadratic and cubic nonlinearities of the dominant $m = 2$ mode source $m = 4$ and $m = 6$ modes with amplitudes scaling like the square and cube of $e^{\mathrm{Im}\,\omega_{222}\,t}$, respectively.

The $\ell = m$ modes in the longitudinal channel also grow until $t \sim 200$, albeit with large and rapid oscillations in the amplitudes. This suggests that the primary stage growth of longitudinal modes is also driven by nonlinear interactions with transverse modes. Indeed, the amplitude of the $m = 2, 4$ and 6 longitudinal modes roughly scales like $e^{\mathrm{Im}\,\omega_{222}\,t}$, $e^{2\mathrm{Im}\,\omega_{222}\,t}$ and $e^{3\mathrm{Im}\,\omega_{222}\,t}$, respectively.

We note that the presence of a growing $m = 2$ longitudinal mode is consistent with our plots of the energy density in Fig. 1, where at $t = 100$ and 220, the dominant excitation was $m = 2$. We also note that at all times studied in this Letter, we see no significant growth in modes with odd values of m. This is consistent with the small growth rates for $m = 3$ appearing in Table I, and with the fact that in perturbation theory an $m = 2$ mode does not source modes with m odd.

We now turn to the secondary growth seen in Fig. 2. Also shown in Fig. 2 as dashed pink lines in the transverse channel are plots of $e^{0.0024t}$ and $e^{0.003t}$ for $m = 2, 4$, respectively. In the longitudinal channel we include plots of $e^{0.0023t}$ and $e^{0.0031t}$ for $m = 2, 4$, respectively, again shown as dashed pink lines. Evidently, after $t \sim 300$ we have $|\mathcal{F}^{232}| \sim e^{0.0024t}$ and $|\mathcal{F}^{122}| \sim e^{0.0023t}$, with $|\mathcal{F}^{122}| \sim 0.3$ at $t = 915$. The $\ell = 5$, $m = 4$ longitudinal mode shows the strongest secondary growth, albeit not purely exponential, with $|\mathcal{F}^{154}| \approx 0.7$ and the approximate tangent $e^{0.0031t}$ at $t = 915$. A large $m = 4$ secondary mode is consistent with our plots of the energy density in Fig. 1, where by $t = 770$ we saw an order

one amplitude $m = 4$ perturbation in the energy density.

It should be emphasized that the growth rates associated with the secondary instability do not coincide with any of the complex frequencies given in Table I. This is to be expected since by the time secondary instabilities kick in, the geometry is very different from Kerr-AdS, from which Table I was obtained.
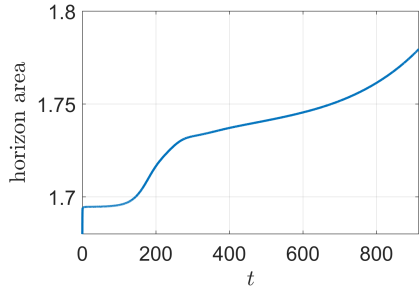

FIG. 3: The apparent horizon area as a function of time. After initial transients decay, the horizon settles down to its Kerr-AdS value 1.694. It subsequently undergoes two distinct periods of growth, with the second period ongoing at $t = 915$.

The distinct primary and secondary growth rates also manifest themselves in the apparent horizon area, which we plot in Fig. 3. After initial transients decay, the horizon area is ≈ 1.694, which is the area of our initial Kerr-AdS black hole. The horizon area grows rapidly around $t \sim 200$ and dramatically slows down after $t \sim 300$. However, by $t \sim 600$, the horizon area growth accelerates again.

What is the physics which leads to two distinct epochs with different instability growth rates? As mentioned above, for given mass and angular momentum there exist hairy black hole solutions with larger entropy than Kerr-AdS, but with only a single *helical* Killing vector [14]

$$K = \partial_t + \mathcal{W}\partial_\varphi, \qquad (3)$$

with $\mathcal{W}$ a constant. Such solutions should naturally be generated by superradiant instabilities when there is a gap in the growth rates, with a single dominant unstable mode [24]. Indeed, for a single mode $e^{-i\omega t + m\varphi}$, Eq. (3) is an approximate Killing vector with

$$\mathcal{W} = \mathrm{Re}(\omega)/m. \qquad (4)$$

From Table I we see that the dominant unstable mode has $\mathrm{Re}(\omega_{222})/2 \approx 1.7$. Black resonators with $\mathcal{W} > 1$ are themselves unstable to superradiant instabilities [15]. Hence, if the primary superradiant instability leads to a black resonator with $\mathcal{W} \approx 1.7$, there should also be a subsequent secondary superradiant instability.

To explore whether our numerics are consistent with a transition to a black resonator, we look for an approximate helical Killing vector. If (3) is a Killing vector,

then the metric and boundary stress tensor should only depend on the combination $\varphi - \mathcal{W}t$, meaning the entire solution rotates at constant angular velocity. Writing $\mathcal{F}^{s\ell m} = |\mathcal{F}^{s\ell m}|e^{i\psi^{s\ell m}}$, we therefore expect phases $\psi^{s\ell m} = -m\mathcal{W}t + \mathrm{const}$. In Fig. 4 we plot $\psi^{s\ell m}/m$ for the same modes shown in Fig. 2. The black dashed line shows the Kerr-AdS prediction $\mathcal{W} = 1.7$. For $100 \lesssim t \lesssim 400$, we see that all curves have the same slope ≈ -1.7. Similar results can be obtained by studying the bulk geometry. Evidently, the dominant transverse $\ell = m = 2$ mode in the Kerr-AdS geometry drives the system to a black resonator configuration with an approximate Killing vector determined by (3) and (4). Given that the associated black resonator has its own superradiant instability, it is natural that we see a secondary instability develop with different growth rates.
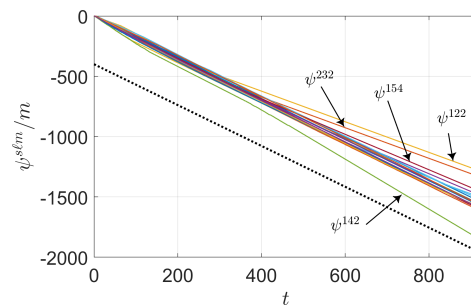

FIG. 4: Phase angles normalized by m for the modes plotted in Fig. 2. All curves have the same slope during $100 \lesssim t \lesssim 400$. The dashed line, shown for reference, has slope -1.7.

What then is the final fate of the system? Does the secondary instability drive the system to another black resonator, with a subsequent black resonator cascade developing as speculated in [16]? To have this happen one presumably needs a gap in the secondary growth rates, so that a single dominant mode $e^{-i\omega t + m\varphi}$ will grow and the solution will have (3) as an approximate Killing vector with $\mathcal{W}$ determined by (4). In contrast to the Kerr-AdS superradiant instability, where the dominant unstable mode grew approximately five times faster than the next subdominant mode, the secondary instabilities we observe don't have a large gap in the growth rates. Indeed, as discussed above, at $t = 915$ we have $|\mathcal{F}^{122}| \sim e^{0.0023t}$ and $|\mathcal{F}^{154}| \sim e^{0.0031t}$. From Fig. 4 we also see that after $t \sim 400$ we have $\psi^{122}/2 \sim -1.27t$ and $\psi^{154}/4 \sim -1.47t$, indicating that these two modes rotate at angular frequencies differing by $\sim 15\%$. This suggests that the secondary instability doesn't lead to another black resonator, but instead to a hairy black hole with no symmetries.

To ascertain the final fate of the system, longer duration simulations must be performed. It should be possible to evolve further using our characteristic evolution scheme, as we see no fundamental problems with the numerics, such as the development of caustics. However, do-

ing so will require lengthy run times due to small growth rates and higher resolutions needed at late times. We leave this for future work.

---

* Electronic address: pchesler@g.harvard.edu
† Electronic address: lowe@brown.edu

[1] Y. B. Zel'dovich, "Generation of waves by a rotating body," *JETP Lett.* **14** (1971) 180.

[2] W. H. Press and S. A. Teukolsky, "Floating Orbits, Superradiant Scattering and the Black-hole Bomb," *Nature* **238** (1972) 211–212.

[3] P. Pani and A. Loeb, "Constraining Primordial Black-Hole Bombs through Spectral Distortions of the Cosmic Microwave Background," *Phys. Rev.* **D88** (2013) 041301, `arXiv:1307.5176 [astro-ph.CO]`.

[4] A. Arvanitaki, M. Baryakhtar, S. Dimopoulos, S. Dubovsky, and R. Lasenby, "Black Hole Mergers and the QCD Axion at Advanced LIGO," *Phys. Rev.* **D95** (2017) no. 4, 043001, `arXiv:1604.03958 [hep-ph]`.

[5] W. E. East and F. Pretorius, "Superradiant Instability and Backreaction of Massive Vector Fields around Kerr Black Holes," `arXiv:1704.04791 [gr-qc]`.

[6] R. Brito, V. Cardoso, and P. Pani, "Superradiance," *Lect. Notes Phys.* **906** (2015) pp.1–237, `arXiv:1501.06570 [gr-qc]`.

[7] J. M. Maldacena, "The Large N limit of superconformal field theories and supergravity," *Int. J. Theor. Phys.* **38** (1999) 1113–1133, `arXiv:hep-th/9711200 [hep-th]`. [Adv. Theor. Math. Phys.2,231(1998)].

[8] S. A. Hartnoll, "Horizons, holography and condensed matter," in *Black holes in higher dimensions*, G. T. Horowitz, ed., pp. 387–419. 2012. `arXiv:1106.4324 [hep-th]`. `http://inspirehep.net/record/914550/files/arXiv:1106.4324.pdf`.

[9] B. Carter, "Hamilton-jacobi and schrödinger separable solutions of einstein's equations," *Comm. Math. Phys.* **10** (1968) no. 4, 280–310. `https://projecteuclid.org:443/euclid.cmp/1103841118`.

[10] V. Cardoso and O. J. C. Dias, "Small Kerr-anti-de Sitter black holes are unstable," *Phys. Rev.* **D70** (2004) 084011, `arXiv:hep-th/0405006 [hep-th]`.

[11] V. Cardoso, O. J. C. Dias, G. S. Hartnett, L. Lehner, and J. E. Santos, "Holographic thermalization, quasinormal modes and superradiance in Kerr-AdS," *JHEP* **04** (2014) 183, `arXiv:1312.5323 [hep-th]`.

[12] N. Sanchis-Gual, J. C. Degollado, P. J. Montero, J. A. Font, and C. Herdeiro, "Explosion and Final State of an Unstable Reissner-Nordström Black Hole," *Phys. Rev. Lett.* **116** (2016) no. 14, 141101, `arXiv:1512.05358 [gr-qc]`.

[13] P. Bosch, S. R. Green, and L. Lehner, "Nonlinear Evolution and Final Fate of Charged Anti–de Sitter Black Hole Superradiant Instability," *Phys. Rev. Lett.* **116** (2016) no. 14, 141102, `arXiv:1601.01384 [gr-qc]`.

[14] Ó. J. C. Dias, J. E. Santos, and B. Way, "Black holes with a single Killing vector field: black resonators," *JHEP* **12** (2015) 171, `arXiv:1505.04793 [hep-th]`.

[15] S. R. Green, S. Hollands, A. Ishibashi, and R. M. Wald, "Superradiant instabilities of asymptotically anti-de Sitter black holes," *Class. Quant. Grav.* **33** (2016) no. 12, 125022, `arXiv:1512.02644 [gr-qc]`.

[16] B. E. Niehoff, J. E. Santos, and B. Way, "Towards a violation of cosmic censorship," *Class. Quant. Grav.* **33** (2016) no. 18, 185012, `arXiv:1510.00709 [hep-th]`.

[17] P. M. Chesler and L. G. Yaffe, "Numerical solution of gravitational dynamics in asymptotically anti-de Sitter spacetimes," *JHEP* **07** (2014) 086, `arXiv:1309.1439 [hep-th]`.

[18] S. de Haro, S. N. Solodukhin, and K. Skenderis, "Holographic reconstruction of space-time and renormalization in the AdS / CFT correspondence," *Commun. Math. Phys.* **217** (2001) 595–622, `arXiv:hep-th/0002230 [hep-th]`.

[19] C. Athanasiou, P. M. Chesler, H. Liu, D. Nickel, and K. Rajagopal, "Synchrotron radiation in strongly coupled conformal field theories," *Phys. Rev.* **D81** (2010) 126001, `arXiv:1001.3880 [hep-th]`. [Erratum: Phys. Rev.D84,069901(2011)].

[20] J. Casalderrey-Solana, M. P. Heller, D. Mateos, and W. van der Schee, "From full stopping to transparency in a holographic model of heavy ion collisions," *Phys. Rev. Lett.* **111** (2013) 181601, `arXiv:1305.4919 [hep-th]`.

[21] P. M. Chesler, N. Kilbertus, and W. van der Schee, "Universal hydrodynamic flow in holographic planar shock collisions," *JHEP* **11** (2015) 135, `arXiv:1507.02548 [hep-th]`.

[22] G. T. Horowitz and J. E. Santos, "Geons and the Instability of Anti-de Sitter Spacetime," *Surveys Diff. Geom.* **20** (2015) 321–335, `arXiv:1408.5906 [gr-qc]`.

[23] V. D. Sandberg, "Tensor spherical harmonics on s^2 and s^3 as eigenvalue problems," *Journal of Mathematical Physics* **19** (1978) no. 12, 2441–2446, `https://doi.org/10.1063/1.523649`.

[24] O. J. C. Dias, G. T. Horowitz, and J. E. Santos, "Black holes with only one Killing field," *JHEP* **07** (2011) 115, `arXiv:1105.4167 [hep-th]`.

[25] Indeed with this choice of n_M we find $n_M n^M = O(10^{-4})$.